



Deep Submillimeter and Radio Observations in the SSA22 Field. I. Powering Sources and the Ly α Escape Fraction of Ly α Blobs

Y. Ao^{1,2}, Y. Matsuda¹, C. Henkel^{3,4}, D. Iono¹, D. M. Alexander⁵, S. C. Chapman⁶, J. Geach⁷, B. Hatsukade⁸, M. Hayes⁹, N. K. Hine¹⁰, Y. Kato^{1,11}, R. Kawabe¹, K. Kohno⁸, M. Kubo¹, M. Lehnert¹², M. Malkan¹³, K. M. Menten³, T. Nagao¹⁴, R. P. Norris^{15,16}, M. Ouchi¹⁷, T. Saito¹⁸, Y. Tamura^{8,19}, Y. Taniguchi²⁰, H. Umehata²⁰, and A. Weiss³

¹National Astronomical Observatory of Japan, 2-21-1 Osawa, Mitaka, Tokyo 181-8588, Japan

²Purple Mountain Observatory, Chinese Academy of Sciences, Nanjing 210008, China

³MPIfR, Auf dem Hügel 69, D-53121 Bonn, Germany

⁴Astron. Dept., King Abdulaziz Univ., P.O. Box 80203, Jeddah 21589, Saudi Arabia

⁵Centre for Extragalactic Astronomy, Department of Physics, Durham University, South Road, Durham DH1 3LE, UK

⁶Dept. of Physics and Atmospheric Science, Dalhousie University, Halifax, NS B3H 4R2, Canada

⁷Centre for Astrophysics Research, University of Hertfordshire, Hatfield, AL10 9AB, UK

⁸Institute of Astronomy, The University of Tokyo, 2-21-1 Osawa, Mitaka, Tokyo 181-0015, Japan

⁹Stockholm University, Department of Astronomy and Oskar Klein Centre for Cosmoparticle Physics, AlbaNova University Centre, SE-10691, Stockholm, Sweden

¹⁰Centre for Astrophysics Research, School of Physics, Astronomy and Mathematics, University of Hertfordshire, College Lane, Hatfield, Hertfordshire AL10 9AB, UK

¹¹Department of Astronomy, Graduate School of Science, The University of Tokyo, 7-3-1 Hongo, Bunkyo-ku, Tokyo 133-0033, Japan

¹²Institut d'Astrophysique de Paris, CNRS and Université Pierre et Marie Curie, 98bis Bd Arago, F-75014 Paris, France

¹³Department of Physics & Astronomy, University of California, Los Angeles, CA 90095, USA

¹⁴Research Center for Space and Cosmic Evolution, Ehime University, Bunkyo-cho 2-5, Matsuyama, Ehime 790-8577, Japan

¹⁵CSIRO Australia Telescope National Facility, P.O. Box 76, Epping, NSW 1710, Australia

¹⁶Western Sydney University, Locked Bag 1797, Penrith South, NSW 1797, Australia

¹⁷Institute for Cosmic Ray Research, The University of Tokyo, 5-1-5 Kashiwa-no-Ha, Kashiwa City, Chiba 277-8582, Japan

¹⁸Nishi-Harima Astronomical Observatory, Centre for Astronomy, University of Hyogo, 407-2 Nichigaichi, Sayo-cho, Sayo, Hyogo 679-5313, Japan

¹⁹Department of Physics, School of Science, Nagoya University, Furo-cho, Chikusa-ku, Nagoya, Aichi 464-8602, Japan

²⁰The Open University of Japan, 2-11, Wakaba, Mihama-ku, Chiba, 261-8586, Japan

Received 2017 April 17; revised 2017 September 11; accepted 2017 October 23; published 2017 November 30

Abstract

We study the heating mechanisms and Ly α escape fractions of 35 Ly α blobs (LABs) at $z \approx 3.1$ in the SSA22 field. Dust continuum sources have been identified in 11 of the 35 LABs, all with star formation rates (SFRs) above $100 M_{\odot} \text{ yr}^{-1}$. Likely radio counterparts are detected in 9 out of 29 investigated LABs. The detection of submillimeter dust emission is more linked to the physical size of the Ly α emission than to the Ly α luminosities of the LABs. A radio excess in the submillimeter/radio-detected LABs is common, hinting at the presence of active galactic nuclei. Most radio sources without X-ray counterparts are located at the centers of the LABs. However, all X-ray counterparts avoid the central regions. This may be explained by absorption due to exceptionally large column densities along the line-of-sight or by LAB morphologies, which are highly orientation dependent. The median Ly α escape fraction is about 3% among the submillimeter-detected LABs, which is lower than a lower limit of 11% for the submillimeter-undetected LABs. We suspect that the large difference is due to the high dust attenuation supported by the large SFRs, the dense large-scale environment as well as large uncertainties in the extinction corrections required to apply when interpreting optical data.

Key words: galaxies: active – galaxies: formation – galaxies: high-redshift – galaxies: ISM – infrared: galaxies

1. Introduction

Ly α emission has emerged as a powerful tool to study distant galaxies, as it is very bright and redshifted to optical wavelengths at high redshifts. Ly α emitters (LAEs), efficiently discovered in narrowband imaging surveys, are galaxies that emit strong Ly α radiation presumably from the photoionization of neutral hydrogen by young, hot stars or active galactic nuclei (AGNs) at high redshifts. They hold unique clues to the formation and evolution of galaxies at a time when the universe was still young (e.g., Bridge et al. 2013). However, due to the resonant nature of the Ly α line and high optical depth in neutral hydrogen (Hayes 2015), Ly α photons are likely to undergo numerous scattering events before they escape from the galaxy or are absorbed by dust. Thus the actual emitted Ly α luminosity is a function of the atomic hydrogen distribution, dust content, gas kinematics, and galaxy viewing angle

(Hayes 2015). Therefore, in order to use Ly α to study galaxies at high redshift, we need to understand the escape fraction of Ly α photons, which is defined as the ratio of observed to intrinsic Ly α luminosity and thus determined by the Ly α emitter's environment. The evolution of the Ly α escape fraction over cosmic time has been determined based on empirical measurements from large samples (e.g., Gronwall et al. 2007; Ouchi et al. 2008; Hayes et al. 2011a), providing useful clues to the evolution of the dust content of galaxies.

As a special class of LAEs, Ly α blobs (LABs) have been most commonly found in the dense environment of star-forming galaxies at high redshift and are characterized by their large physical scale (30–200 kpc) and high Ly α luminosity (10^{43} – 10^{44} erg s $^{-1}$; see e.g., Francis et al. 1996; Steidel et al. 2000; Matsuda et al. 2004, 2009, 2011, 2012; Palunas et al. 2004; Dey et al. 2005; Saito et al. 2006; Yang et al. 2009, 2010; Erb et al. 2011; Prescott et al. 2012a,

2013; Bridge et al. 2013). While the LABs' preferential location in over-dense environments indicates an association with massive galaxy formation, the origin of their Ly α emission is still unclear and under debate (Faucher-Giguère et al. 2010; Cen & Zheng 2013; Yajima et al. 2013). Proposed sources have generally fallen into two categories: (1) cooling radiation from cold streams of gas accreting onto galaxies (e.g., Haiman et al. 2000; Dijkstra & Loeb 2009; Faucher-Giguère et al. 2010) and (2) photoionization and/or galactic superwinds/outflows from starbursts or AGNs (e.g., Taniguchi & Shioya 2000; Furlanetto et al. 2005; Wilman et al. 2005; Colbert et al. 2006; Mori & Umemura 2006; Matsuda et al. 2007; Zheng et al. 2011; Cen & Zheng 2013; Ao et al. 2015; Prescott et al. 2015; Alexander et al. 2016; Hine et al. 2016). All of the above mentioned energy supplying sources may trigger Ly α emission in an environment where violent interactions are frequent between gas rich galaxies as expected in over-dense regions at high redshift (Matsuda et al. 2009, 2011; Prescott et al. 2012a, 2013; Kubo et al. 2013).

Supporting evidence for the cooling flow scenario comes from those LABs lacking any visible power source (e.g., Smith & Jarvis 2007). Dijkstra & Loeb (2009) demonstrates that if >10% of the change in the gravitational binding energy of a cold flow goes into heating of the gas, then the simulated cooling flows are spatially extended Ly α sources that are comparable to observed LABs. This model can naturally explain the spatial distribution of the LABs and the diversity of host galaxies in the LABs, as the Ly α emission is effectively decoupled from the associated sources. The most luminous gravitationally powered blobs would be associated with the most massive halos, which may host a variety of sources like AGNs, Lyman break galaxies (LBGs), and submillimeter galaxies (SMGs). Alternatively, ionizing photons from young stars in star-forming (SF) galaxies and/or unobscured AGNs can ionize neutral hydrogen atoms and the subsequent recombination leads to Ly α emission. It is usually difficult to discriminate between the two internal heating mechanisms, SF or AGNs. Resonant scattering of Ly α photons in the circumgalactic medium leads to spatially extended emission (Geach et al. 2005, 2009; Colbert et al. 2006; Webb et al. 2009; Hayes et al. 2011b; Zheng et al. 2011; Cen & Zheng 2013; Overzier et al. 2013). Cen & Zheng (2013) propose an SF-based model and predict that LABs at high redshift correspond to protoclusters containing the most massive galaxies/halos in the universe and ubiquitous strong infrared (IR) sources undergoing extreme starbursts. Their model also predicts that the most luminous FIR source within each LAB is likely representing the gravitational center of the protocluster. Note that both cooling flow (Dijkstra & Loeb 2009) and SF-based models (Cen & Zheng 2013) can reproduce the measured luminosity functions of LABs.

To study the heating mechanism(s) of the LABs and investigate their Ly α escape fraction, we need to select a large sample of LABs to locate their accurate positions and investigate their possible powering sources. SSA22 is such a suitable field because it has 35 LABs detected at $z \approx 3.1$ (Matsuda et al. 2004), providing an ideal laboratory to study the LABs in a large sample. One of them, SSA22-LAB01 is the best studied source (e.g., Matsuda et al. 2007; Yang et al. 2012; Geach et al. 2014, 2016; Umehata et al. 2017a). At (sub) millimeter wavelength, most LABs of SSA22 have been

studied with the Submillimetre Common-User Bolometer Array (SCUBA, Geach et al. 2005) and SCUBA-2 (Hine et al. 2016) on the James Clerk Maxwell Telescope (JCMT), and with the AzTEC 1.1 mm camera (Tamura et al. 2009, 2013; Umehata et al. 2014) on the Atacama Submillimeter Telescope Experiment (ASTE). However, no significant 1.1 mm continuum has been found in any of the individual 35 LABs (Tamura et al. 2013). Even in the recent deep SCUBA-2 observations, only 2 out of 34 LABs are detected at 850 μm (Hine et al. 2016). A few LABs have been observed and detected in the dust continuum with the Atacama Large Millimeter/Submillimeter Array (ALMA; Umehata et al. 2015; Alexander et al. 2016; Geach et al. 2016). In this paper, we present deep submillimeter results from new JCMT/SCUBA-2 data (Holland et al. 2013) together with ALMA data, and deep radio images from the Karl G. Jansky Very Large Array (VLA)²¹ observations to study the LABs in the SSA22 field. Note that in this paper we only focus on the LABs; the SMGs in this region will be presented in an upcoming paper based on the same submillimeter and radio data (Y. Ao et al. 2017, in preparation).

2. Observations

2.1. JCMT/SCUBA-2 Observations

The observations were carried out at 850 μm with SCUBA-2 (Holland et al. 2013) at the JCMT. The data were taken between 2015 April 20 and June 30 under good weather conditions when the zenith optical depth at 225 GHz was in the range of $0.04 < \tau_{225} < 0.08$ with a mean $\langle \tau_{225} \rangle$ of 0.06. We observed a subregion of SSA22 with a total on-source observing time of 19 hr, covering a field with a diameter of 15 arcmin, centered on $\alpha(\text{J2000}) = 22^{\text{h}}17^{\text{m}}31^{\text{s}}.7$, $\delta(\text{J2000}) = +00^{\circ}17'50''$, using multiple repeats (40 minutes per repeat) of the PONG scanning pattern (Holland et al. 2013). The SSA22 field was also observed as part of the JCMT SCUBA-2 Cosmology Legacy Survey (S2CLS, Hine et al. 2016; Geach et al. 2017) with a total on-source observing time of 72 hr to cover a map with a diameter of 30 arcmin, centered on $\alpha(\text{J2000}) = 22^{\text{h}}17^{\text{m}}36^{\text{s}}.3$, $\delta(\text{J2000}) = +00^{\circ}19'22''.7$. The observations are summarized in Table 1.

Pointing checks and flux calibration were achieved via observations of Neptune and Uranus, immediately before and after the science exposures. Data reduction was carried out using the Submillimeter User Reduction Facility (smurf) *makemap* pipeline (Chapin et al. 2013), with flat fields, image stacking, and removing atmospheric emission (see also Hine et al. 2016 for more details). The main beam size of the SCUBA-2 observations at 850 μm is 14'' and the map is convolved with a smoothed beam of 30'' to optimize the detection of point sources. The total on-source integration time was about 91 hr (see Table 1). The final beam-convolved map reaches an rms noise level of 0.75 mJy/beam within the central 15 arcmin and about 1.0 mJy/beam outside the central region (see Figure 1).

²¹ The National Radio Astronomy Observatory is a facility of the National Science Foundation operated under cooperative agreement by Associated Universities, Inc.

Table 1
Observation Logs in SSA22

Telescope	Observation Date	Project	R.A. (J2000)	Decl. (J2000)	Freq. (GHz)	Map Size ^a (arcmin)	Observing Time (hr)	On-source Time (hr)
JCMT/SCUBA-2	2012 Sep–2013 Dec	MJLSC02	22:17:36.30	+00:19:22.7	345	30	...	72
JCMT/SCUBA-2	2015 Apr–2015 Jun	M15AI91	22:17:31.70	+00:17:50.0	345	15	...	19
VLA	2015 Apr–2015 Apr	15A-120	22:17:28.00	+00:17:50.0	2–4	15	6.7	4.2
VLA	2016 May–2016 May	16A-310	22:17:43.00	+00:10:40.0	2–4	15	2	1.6
VLA	2016 May–2016 Aug	16A-310	22:17:32.00	+00:15:00.0	2–4	15	32	26.1

Note. Note that the best sensitivities in the images are 0.75 mJy/beam for the combined SCUBA-2 observations and 1.5 μ Jy/beam for the combined VLA observations, respectively.

^a The map size of the VLA observations is the field of view at the central frequency of 3 GHz.

2.2. ALMA Observations

ALMA observations were carried out in band 7 with a central frequency of 350 GHz toward 4 LABs (LAB1, LAB2, LAB5, and LAB18; project code: 2013.1.00704S; Y. Matsuda et al. 2017, in preparation). Another two LABs, LAB12 and LAB14, had been covered by a deep field in SSA22 (Umehata et al. 2015, 2017b) in band 6 with a central frequency of 263 GHz. The data were reduced with the CASA package in a standard manner (for details, see Umehata et al. 2017b and Y. Matsuda et al. 2017, in preparation).

2.3. VLA Observations

We observed the SSA22 region centered around the location of our SCUBA-2 observations with the VLA in B-configuration at S-band (2–4 GHz), under projects 15A-120 and 16A-310. During 17 sessions with a total observing time of 41 hr, we observed three positions in 2015 and 2016 (see Table 1 for the observing log). The total bandwidth was 2 GHz, split into 16 spectral windows.

Data were first processed through the VLA Common Astronomy Software Applications (CASA) Calibration Pipeline by NRAO staff, performing basic flagging and calibration. Then we iteratively inspected the data, and then flagged the data with radio frequency interference. The final mosaic of images was created with CASA task CLEAN, reaching an rms sensitivity of 1.5 μ Jy/beam (before primary beam correction) and an angular resolution of $2''.3 \times 2''.0$. The primary beam of one single pointing is about 15 arcmins. In Figure 2, we indicate the locations of 29 out of the 35 LABs identified by Y. Matsuda et al. (2004) in the final radio image.

3. Results

3.1. Submillimeter Emission

For the 35 LABs identified in Matsuda et al. (2004), all sources are covered by SCUBA-2 observations, as shown in Figure 1. The SSA22 field has been observed as part of the JCMT S2CLS project (Geach et al. 2017), reaching a 1σ level of 1.1 mJy/beam at 850 μ m. Combined with our SCUBA2 observations in 2015, we reach a deeper rms sensitivity of about 0.75 mJy/beam for the overlapping region.

The SCUBA-2 850 μ m flux measurements are listed in Table 2. Out of the 35 LABs, 9 are detected in dust emission with peak signal-to-noise ratios (S/Ns) above 2.5σ , and 6 of them above 3σ (see Figure 3). The three sources, LAB4, LAB9, and LAB14, with only marginal detection levels of 2.5σ , have all been detected in the radio above 5σ .

Figure 4 shows the SCUBA-2, VLA, and ALMA images together to cross-check the detections with low significance from the SCUBA-2 and VLA observations by the highly significant ones from ALMA. The typical pointing accuracy of the JCMT is about $1''$ – $2''$. Due to the noise of the image, the positional uncertainty of the SCUBA-2 observations is related to its S/N and beam size (Condon et al. 1998) via $\sigma_p = \frac{\theta_{\text{beam}}}{S/N(2\ln 2)^{0.5}}$, where σ_p is the 1σ positional uncertainty and θ_{beam} the beam size. For a marginally detected source with an S/N of 3 and a smoothed beam of $30''$, its positional uncertainty will be about $8''.5$. Six LABs observed by ALMA have been detected with high S/Ns. Two sources, LAB2 and LAB12, have not been detected with SCUBA-2 due to low flux densities, but have been detected with ALMA in the dust continuum. For the remaining four LABs, their positions are consistent with our SCUBA-2 observations if considering the positional uncertainties of SCUBA-2 observations. The VLA positions of the radio emission are in good agreement with those of the dust emission obtained with ALMA. These consistent results support the reliability of the SCUBA-2 and VLA data, even for the marginal detections. Adopting the number count study of SCUBA-2 sources in Geach et al. (2017), the probability of finding a 850 μ m source with a flux greater than 2 mJy within a box of $15''$, accounting for the typical LAB's size and the SCUBA-2's beam size at 850 μ m, is $\sim 5.2\%$. Thus, we expect to have two spurious submillimeter sources detected above 2 mJy among the 35 LABs in the SSA22 field. However, all SCUBA-2-detected sources have significant radio counterparts except for LAB10 and LAB11. The former is not covered by the VLA observations and the latter has a weak radio counterpart. Thus, all SCUBA-2 sources are very likely associated with the LABs, instead of merely representing chance coincidences along the given lines of sight.

Previously, three deep (sub)millimeter surveys had been carried out in this field (Geach et al. 2005, 2017; Tamura et al. 2013; Hine et al. 2016) and their results are presented in Table 2. Early SCUBA data (Geach et al. 2005) show five sources detected at $\geq 3.5\sigma$. However, only two sources, LAB1 and LAB18, have been confirmed by the recent deeper SCUBA2 observations (Hine et al. 2016). Our results are consistent with those in Hine et al. (2016). For the LABs detected in Geach et al. (2005), we confirmed all sources but mostly with much lower flux densities. The large difference may be due to flux boosting in the original SCUBA data and issues related to data reduction and calibrations (Hine et al. 2016). Adopting the SED templates described in Section 3.3, one expects that flux densities at 1.1 mm are about half of those at 850 μ m. Thus, it is not surprising that

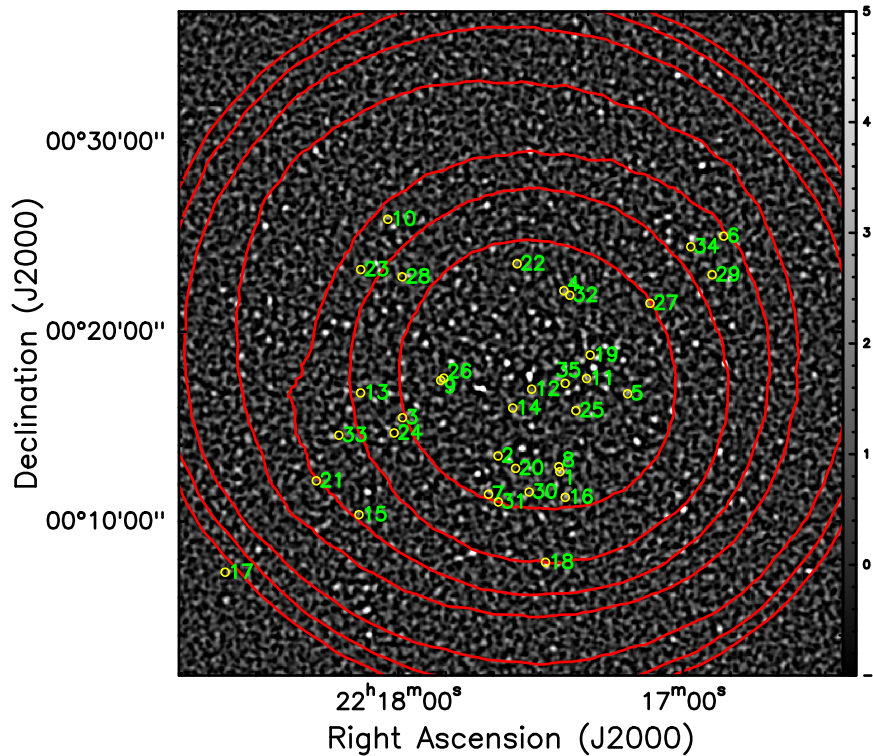


Figure 1. Signal-to-noise map of the SCUBA-2 data in the SSA22 region in gray is overlaid with contour levels of 0.8, 0.9, 1.0, 1.1, 1.3, 1.5, and 1.7 mJy/beam of the noise map. The locations of the 35 LABs identified by Matsuda et al. (2004) are shown as yellow circles with diameters of 25 arcsec. The ID numbers of the sources are indicated in green.

none of the LABs is individually detected at $\geq 3.5\sigma$ at 1.1 mm by AzTEC/ASTE (Tamura et al. 2013). Typical predicted fluxes of SCUBA2-detected LABs are less than 1.5 mJy at 1.1 mm, which corresponds to about 2σ . Actually, the brightest source, LAB18, is the only 3σ detection at 1.1 mm, and is consistent with the predicted value from the SED templates.

We also stack the remaining submillimeter-undetected LABs except for LAB17, because the latter is located in a region with a high noise level (see Figure 1). The stacked image shows no significant detection at $>3\sigma$ (0.56 mJy).

3.2. Radio Emission

In Figure 2, we show the full radio map imaged by the VLA observations with the radio emission in grayscale. Twenty-nine sources are covered by our observations, and 7 (LAB13, LAB15, LAB21, LAB22, LAB27, LAB28, and LAB33) of them are outside the central field of view (FoV) with a noise level of above $\sim 3.5 \mu\text{Jy}/\text{beam}$ after primary beam correction. None of the sources outside of the FoV are detected at radio wavelengths, and this may well be related to the lower sensitivity in these regions. Among the remaining 22 LABs, 9 are detected above 4σ . The VLA S-band flux measurements are listed in Table 2. For 5 out of 9 radio-detected sources, spectroscopic data from the literature at the same locations as the radio counterparts show that their redshifts are around 3.1 (see Table 2). Adopting the number count study of radio sources in Condon et al. (2012), the probability of finding a 3 GHz source with a flux greater than $7.5 \mu\text{Jy}$ within a typical LAB's size of $6''$ is $\sim 4.2\%$. Thus, among the 22 sources with good sensitivities, we expect to have one spurious radio source detected above $7.5 \mu\text{Jy}$.

3.3. Star Formation Rates (SFRs)

Here we derive the SFRs from the $\text{Ly}\alpha$, IR, and radio luminosities. To estimate the SFR from the $\text{Ly}\alpha$ luminosity, we first assume that star formation (SF) powers the observed $\text{Ly}\alpha$ flux. We use an unreddened $\text{Ly}\alpha/\text{H}\alpha$ ratio of 8.7:1 and the conversion factor between $\text{H}\alpha$ luminosity and SFR (Kennicutt 1998; Kennicutt & Evans 2012), yielding $\text{SFR}(\text{Ly}\alpha)/(M_{\odot} \text{yr}^{-1}) = 0.62 \times L_{\text{Ly}\alpha}/(10^{42} \text{ erg s}^{-1})$. This provides a lower limit, because the dust extinction of $\text{Ly}\alpha$ emission, likely exacerbated by resonance scattering, may significantly reduce the observed $\text{Ly}\alpha$ luminosity.

For another estimate of the SFR, we first need to determine the IR luminosity. However, the dust SEDs of the LABs cannot be well constrained, as only one or two measurements at (sub) millimeter wavelengths are available. Therefore, we will follow the method described in Umehata et al. (2015) to use SED templates of well studied starburst galaxies, Arp 220 and M82 (Silva et al. 1998), a composite SED of SMGs from the ALMA LESS survey (ALESS, Swinbank et al. 2014) and SMM J21350201 (the cosmic eyelash; Swinbank et al. 2010) to consider a variety of SEDs. We created best-fit SEDs for each template based on redshift and SCUBA-2/ALMA measurements. The spectra between 8 and $1000 \mu\text{m}$ in the rest frame were integrated, and we derive a median value as well as minimum/maximum values. Following the SFR calibration in Kennicutt (1998) and Kennicutt & Evans (2012), we can estimate the SFR by using the relation $\text{SFR}(L_{\text{FIR}})/(M_{\odot} \text{yr}^{-1}) = 1.46 \times L_{\text{FIR}}/(10^{10} L_{\odot})$. The uncertainties of submillimeter-derived SFRs mainly come from the choice of adopted templates, and the minimum and maximum as well as median values are given in Table 3.

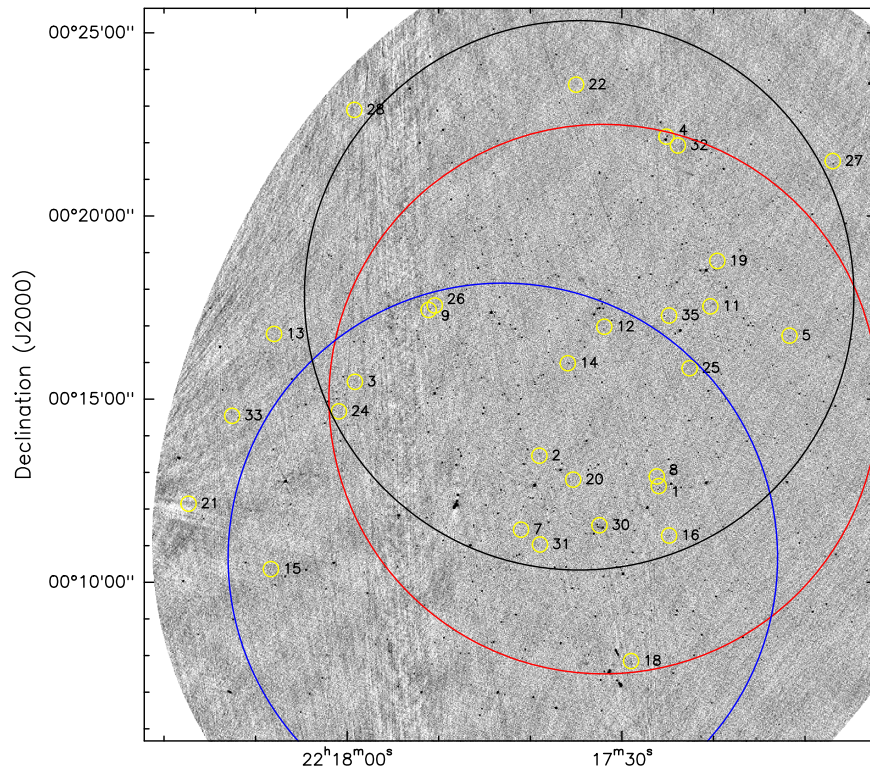


Figure 2. Radio map of the SSA22 region in grayscale. Three big circles denote the primary full width at half maximum beam size for three pointings with different on-source observing times (red: 26 hr, blue: 1.6 hr, and black: 4.2 hr). The locations of 29 out of the 35 LABs identified by Matsuda et al. (2004) are covered by our observations and are shown as yellow circles with diameters of 25 arcsec. The ID numbers of the sources are labeled in black.

In luminous galaxies, radio emission is dominated by synchrotron radiation from electrons, and one can relate this emission to the SFR by $\text{SFR}(L_{1.4 \text{ GHz}})/(M_{\odot} \text{ yr}^{-1}) = 5.52 \times 10^{-22} L_{1.4 \text{ GHz}}/(\text{W Hz}^{-1})$ (Bell 2003). The radio luminosity at 1.4 GHz in the rest frame can be estimated from the observed flux at 3 GHz by assuming a relation $S \propto \nu^{\alpha}$, where S is the flux density and a typical spectral index commonly adopted for SMGs (e.g., Ivison et al. 2010) is $\alpha = -0.8$. The SFRs derived using these three methods are listed in Table 3.

3.4. Comments on Individual LABs

Radio data are not only helpful to discover the powering sources, but also to provide accurate positions of the unresolved SCUBA-2-detected sources and help to cross-identify and even verify the corresponding dust emission at a relatively faint detection level. Here, we will briefly describe the sources detected at submillimeter and radio wavelengths. Deep X-ray observations with *Chandra* are available for the SSA22 field (Geach et al. 2009; Lehmer et al. 2009), and will also be discussed for the detected sources. For those readers mainly interested in statistically relevant results, we recommend continuing with Section 4.

3.4.1. LAB1

For LAB1, the ALMA observations at 850 μm reveal three cores with a total flux density of 1.72 ± 0.21 mJy (upper left panel in Figure 4; see also Geach et al. 2016), two close to VLA-LAB1a and one close to VLA-LAB1b. Using the SCUBA-2 data, Geach et al. (2014) found a flux density of 4.6 ± 1.1 mJy. Not accounting for the slightly different

SCUBA-2 and ALMA primary beams, this suggests that $63\% \pm 10\%$ of the extended emission is missed by the ALMA observations. Combining this with our new SCUBA-2 data, we find a flux density of 2.9 ± 0.8 mJy, indicating that missing flux accounts for $41\% \pm 15\%$ of the total flux density. Considering the flux uncertainties, the new value is only slightly higher than ALMA’s measurement, showing that in this LAB there may be not much extended structure missed by ALMA. Adopting the SED templates described in Section 3.3, the predicted flux densities are $0.46^{+0.40}_{-0.12}$ mJy for ALMA-LAB1ab, $0.27^{+0.24}_{-0.07}$ mJy for ALMA-LAB1c at 1.25 mm, and $0.025^{+0.022}_{-0.007}$ mJy for ALMA-LAB1 at 3.5 mm, respectively. These results are consistent with the 3σ upper limits around LAB1 of 0.45 mJy at 1.25 mm and 0.15 mJy at 3.5 mm reported by Yang et al. (2012).

Two radio sources are detected in this LAB. The northern radio source, VLA-LAB1a, peaks at a location close to two dust continuum peaks, ALMA-LAB1a and ALMA-LAB1b. The southern radio source, VLA-LAB1b, is consistent with one of the ALMA 350 GHz continuum sources, ALMA-LAB1c. Weak X-ray emission is detected around the southern source. [C II] emission has also been detected in ALMA-LAB1b with a secured redshift of 3.0993 ± 0.0004 (Umehata et al. 2017b).

3.4.2. LAB2

Radio emission is detected within this LAB. However, SCUBA-2 observations show no dust emission around this source down to a 2σ level of 1.6 mJy. Sensitive ALMA observations find a counterpart near the radio source with a flux

Table 2
JCMT/SCUBA-2 and VLA S-band Observations toward LABs in SSA22

Source	R.A.(J2000)	Decl.(J2000)	$S_{850 \mu\text{m}}^a$ (mJy)	Previous (sub)mm Measurements ^b			VLA Observations ^c					Spectroscopic Observations ^d			References
				$S_{850 \mu\text{m}}$ (mJy) Geach et al. (2005)	$S_{850 \mu\text{m}}$ (mJy) Hine et al. (2016)	$S_{1.1 \text{ mm}}$ (mJy) Tamura et al. (2013)	VLA ID	rms (μJy)	offx ($''$)	offy ($''$)	$S_{10 \text{ cm}}$ (μJy)	offx ($''$)	offy ($''$)	zred	
SCUBA2-LAB1	22:17:25.961	+00:12:37.57	2.9 ± 0.8	16.8 ± 2.9	4.6 ± 1.1	1.97 ± 0.74
ALMA-LAB1ab	22:17:25.981	+00:12:36.35	1.08 ± 0.17	VLA-LAB1a	1.64/1.79	-0.4	-1.1	7.3 ± 2.2
ALMA-LAB1c	22:17:26.100	+00:12:32.37	0.64 ± 0.12	VLA-LAB1b	1.64/1.79	0.2	-0.1	8.6 ± 2.2	0.0	-0.1	3.0993+/-0.0004	(1)
ALMA-LAB1	1.72 ± 0.21
SCUBA2-LAB2	22:17:38.996	+00:13:27.51	-0.5 ± 0.8	3.3 ± 1.2	0.1 ± 1.1	-1.89 ± 0.76
ALMA-LAB2	22:17:39.079	+00:13:30.85	0.91 ± 0.10	VLA-LAB2	1.57/1.65	0.0	0.0	8.4 ± 2.4	-0.5	-0.7	3.091+/-0.001	(3)
SCUBA2-LAB3	22:17:59.153	+00:15:28.37	0.2 ± 0.9	-0.2 ± 1.5	0.1 ± 1.1	-0.69 ± 0.73	VLA-LAB3	1.54/2.70	-1.9	-1.8	7.5 ± 3.8
SCUBA2-LAB4	22:17:25.126	+00:22:10.21	2.4 ± 0.8	0.9 ± 1.5	2.4 ± 1.1	0.11 ± 0.74	VLA-LAB4a	1.48/2.72	0.0	0.1	25.4 ± 4.1
SCUBA2-LAB5	22:17:11.681	+00:16:43.95	2.9 ± 0.8	5.2 ± 1.4	1.9 ± 1.1	0.34 ± 0.74
ALMA-LAB5	22:17:11.664	+00:16:44.32	2.21 ± 0.08	VLA-LAB5	1.29/1.93	0.1	-0.4	10.8 ± 2.7
SCUBA2-LAB6	22:16:51.428	+00:25:02.39	0.4 ± 1.0	-0.5 ± 1.8	1.0 ± 1.1	0.07 ± 1.14	...	n.a.
SCUBA2-LAB7	22:17:41.005	+00:11:26.32	-1.0 ± 0.8	0.2 ± 1.6	1.2 ± 1.1	-0.88 ± 0.74	...	1.52/1.81
SCUBA2-LAB8	22:17:26.176	+00:12:53.53	-0.6 ± 0.8	0.3 ± 5.3	2.6 ± 1.1	0.67 ± 0.74	...	1.65/1.78
SCUBA2-LAB9	22:17:51.084	+00:17:26.31	2.2 ± 0.8	1.3 ± 5.3	2.2 ± 1.1	0.07 ± 0.74	VLA-LAB9a	1.54/2.25	-2.0	0.7	11.1 ± 3.4
SCUBA2-LAB10	22:18:02.250	+00:25:55.77	2.7 ± 1.1	6.1 ± 1.4	3.2 ± 1.1	1.20 ± 0.84	...	n.a.
SCUBA2-LAB11	22:17:20.325	+00:17:32.05	2.3 ± 0.7	-0.4 ± 5.3	2.5 ± 1.1	0.61 ± 0.73	VLA-LAB11	1.46/1.78	-1.8	2.9	5.5 ± 2.7
SCUBA2-LAB12	22:17:31.907	+00:16:58.77	0.7 ± 0.8	3.2 ± 1.6	0.8 ± 1.1	0.30 ± 0.74
ALMA-LAB12	22:17:32.01	+00:16:55.4	0.63 ± 0.03	VLA-LAB12	1.61/1.70	0.2	0.1	7.4 ± 2.4	-0.2	0.1	3.0909+/-0.0004	(2)
SCUBA2-LAB13	22:18:07.972	+00:16:46.77	0.1 ± 0.9	...	1.2 ± 1.1	-0.72 ± 0.73	...	1.32/3.95
SCUBA2-LAB14	22:17:35.908	+00:15:58.79	2.0 ± 0.7	4.9 ± 1.3	2.0 ± 1.1	2.43 ± 0.76
ALMA-LAB14	22:17:35.83	+00:15:59.0	1.45 ± 0.09	VLA-LAB14	1.51/1.54	0.1	-0.4	14.5 ± 2.1	1.0	0.0	3.094	(4)

9

Table 2
(Continued)

Source	R.A.(J2000)	Decl.(J2000)	$S_{850\ \mu\text{m}}^{\text{a}}$ (mJy)	Previous (sub)mm Measurements ^b			VLA Observations ^c					Spectroscopic Observations ^d			References
				$S_{850\ \mu\text{m}}$ (mJy) Geach et al. (2005)	$S_{850\ \mu\text{m}}$ (mJy) Hine et al. (2016)	$S_{1.1\ \text{mm}}$ (mJy) Tamura et al. (2013)	VLA ID	rms (μJy)	offx ($''$)	offy ($''$)	$S_{10\ \text{cm}}$ (μJy)	offx ($''$)	offy ($''$)	zred	
SCUBA2-LAB15	22:18:08.317	+00:10:21.78	1.3 ± 1.1	...	2.4 ± 1.1	-0.27 ± 0.74	...	1.51/4.33
SCUBA2-LAB16	22:17:24.845	+00:11:16.77	2.4 ± 0.8	2.2 ± 5.3	3.4 ± 1.1	0.34 ± 0.74	VLA-LAB16	1.44/1.77	0.2	0.6	8.5 ± 2.7	0.8	0.7	$3.0689+/-0.0002$	(2)
SCUBA2-LAB17	22:18:36.533	+00:07:19.88	-1.5 ± 1.9	1.41 ± 1.19	...	n.a.
SCUBA2-LAB18	22:17:28.998	+00:07:51.16	5.4 ± 0.9	11.0 ± 1.5	5.2 ± 1.1	2.33 ± 0.73
ALMA-LAB18a	22:17:29.032	+00:07:50.26	1.18 ± 0.08	VLA-LAB18a	1.58/2.80	-0.2	0.1	13.0 ± 4.2
ALMA-LAB18b	22:17:28.936	+00:07:46.92	2.73 ± 0.10	VLA-LAB18b	1.58/2.80	-0.1	0.0	9.1 ± 4.0
ALMA-LAB18c	22:17:29.017	+00:07:43.44	1.14 ± 0.15	1.58/2.80
ALMA-LAB18d	22:17:28.781	+00:07:40.07	4.42 ± 0.30	VLA-LAB18d	1.58/2.80	0.2	0.4	16.4 ± 4.3
ALMA-LAB18	9.47 ± 0.36
SCUBA2-LAB19	22:17:19.569	+00:18:46.38	-2.1 ± 0.7	-8.6 ± 5.3	-0.4 ± 1.1	-0.81 ± 0.74	...	1.56/2.09
SCUBA2-LAB20	22:17:35.307	+00:12:48.31	-0.4 ± 0.8	0.4 ± 1.5	0.2 ± 1.1	-0.80 ± 0.75	...	1.60/1.68
SCUBA2-LAB21	22:18:17.324	+00:12:08.66	1.1 ± 1.2	...	0.9 ± 1.1	-1.37 ± 0.75	...	1.63/6.63
SCUBA2-LAB22	22:17:34.982	+00:23:35.09	1.5 ± 0.8	...	1.3 ± 1.1	1.04 ± 0.74	...	1.31/3.45
SCUBA2-LAB23	22:18:07.950	+00:23:16.62	-0.1 ± 1.1	...	1.0 ± 1.1	-1.55 ± 0.80	...	n.a.
SCUBA2-LAB24	22:18:00.905	+00:14:40.10	-0.9 ± 0.8	...	-0.6 ± 1.1	0.03 ± 0.72	...	1.64/2.93
SCUBA2-LAB25	22:17:22.590	+00:15:50.86	-2.1 ± 0.8	1.4 ± 5.3	-1.5 ± 1.1	0.01 ± 0.73	...	1.43/1.57
SCUBA2-LAB26	22:17:50.424	+00:17:33.37	0.6 ± 0.8	-2.7 ± 5.3	1.1 ± 1.1	-0.90 ± 0.74	...	1.50/2.17
SCUBA2-LAB27	22:17:06.974	+00:21:30.15	1.7 ± 0.8	0.5 ± 1.6	2.1 ± 1.1	0.18 ± 0.77	...	1.29/3.70
SCUBA2-LAB28	22:17:59.210	+00:22:53.96	-0.1 ± 0.9	...	-0.6 ± 1.1	-0.99 ± 0.76	...	1.41/5.83
SCUBA2-LAB29	22:16:53.869	+00:23:00.39	0.3 ± 1.1	...	0.7 ± 1.1	-2.54 ± 0.91	...	n.a.
SCUBA2-LAB30	22:17:32.454	+00:11:33.36	0.6 ± 0.9	3.3 ± 1.3	1.9 ± 1.1	0.65 ± 0.74	VLA-LAB30a	1.72/1.91	4.6	1.6	24.9 ± 2.4
	VLA-LAB30b	1.72/1.91	1.1	0.7	4.3 ± 2.4
	VLA-LAB30c	1.72/1.91	3.4	-2.5	20.0 ± 2.6

Table 2
(Continued)

Source	R.A.(J2000)	Decl.(J2000)	$S_{850 \mu\text{m}}^{\text{a}}$ (mJy)	Previous (sub)mm Measurements ^b			VLA Observations ^c				Spectroscopic Observations ^d			References	
				$S_{850 \mu\text{m}}$ (mJy) Geach et al. (2005)	$S_{850 \mu\text{m}}$ (mJy) Hine et al. (2016)	$S_{1.1 \text{ mm}}$ (mJy) Tamura et al. (2013)	VLA ID	rms (μJy)	offx ($''$)	offy ($''$)	$S_{10 \text{ cm}}$ (μJy)	offx ($''$)	offy ($''$)		zred
SCUBA2-LAB31	22:17:38.945	+00:11:01.87	-0.7 ± 0.8	-3.7 ± 5.3	0.0 ± 1.1	-1.44 ± 0.74	VLA-LAB30d	1.72/1.91	-4.8	-3.7	46.9 ± 2.6
SCUBA2-LAB32	22:17:23.874	+00:21:55.46	0.6 ± 0.7	1.8 ± 1.4	0.9 ± 1.1	-0.16 ± 0.74	...	1.48/1.78
SCUBA2-LAB33	22:18:12.553	+00:14:32.67	-0.6 ± 1.1	1.6 ± 1.5	0.7 ± 1.1	0.04 ± 0.73	...	1.41/4.92
SCUBA2-LAB34	22:16:58.365	+00:24:29.08	-0.7 ± 1.1	...	0.4 ± 1.1	1.01 ± 0.93	...	n.a.
SCUBA2-LAB35	22:17:24.837	+00:17:16.92	-0.3 ± 0.8	1.2 ± 5.3	1.0 ± 1.1	-0.74 ± 0.73	...	1.58/1.77

Notes.

^a The fluxes are measured at $850 \mu\text{m}$ by JCMT/ALMA except for LAB12 and LAB14. The latter two sources were observed at 1.14 mm with ALMA (Umehata et al. 2015). The sources detected at submillimeter wavelengths are highlighted in bold font.

^b Previous (sub)millimeter measurements from three deep surveys. The first two were carried out at $850 \mu\text{m}$ by SCUBA (Geach et al. 2005) and SCUBA2 (Hine et al. 2016), respectively. The third one was taken at 1.1 mm by AzTEC/ASTE (Tamura et al. 2013). Sources detected with S/Ns at $\geq 3.5\sigma$ are shown in bold font.

^c In Column 9, the given two values are for the noise levels before and after primary beam correction. The offsets of radio counterparts relative to the LAB centers or ALMA sources are given in Columns 7 and 8. The counterparts associated with the LABs are highlighted in bold font.

^d Only the targets with offsets (Column 13 and 14) less than 1 arcsec relative to the radio sources are considered to be associated with the radio sources. References: (1) Umehata et al. (2017b); (2) Kubo et al. (2015); (3) Steidel et al. (2003); (4) Yamada et al. (2012).

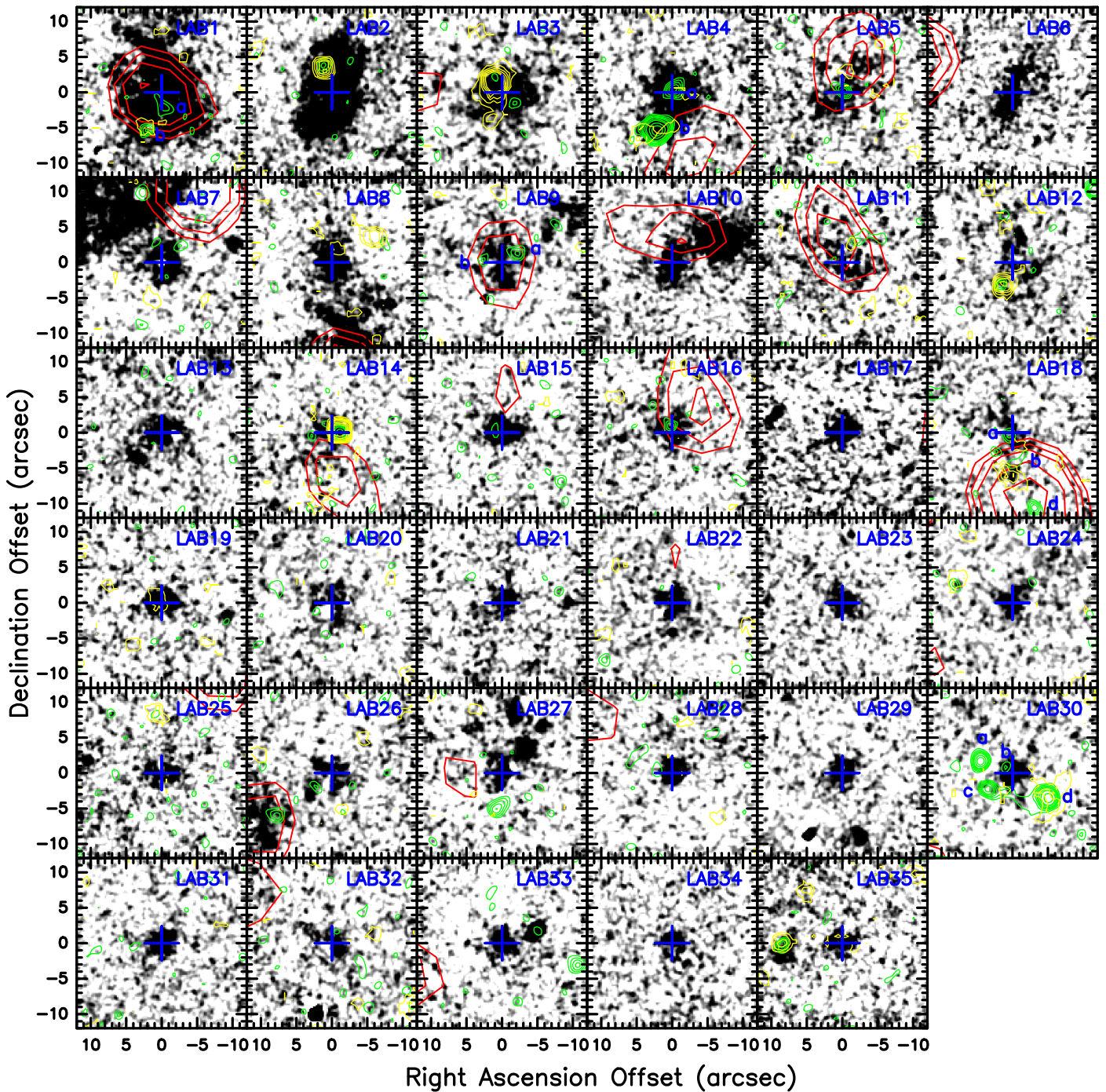


Figure 3. SCUBA2 dust emission at $850\ \mu\text{m}$ in red (the contour levels are 2, 2.5, 3, 4, and 5 times the respective noise level, the latter given in Column 4 of Table 2), VLA radio emission at 3 GHz in green (contour levels are 2, 3, 4, 5, 6, 8, 10, 15, 20, and 30σ and the values of σ are the noise levels prior to primary beam correction given in Column 6 of Table 2) and *Chandra* X-ray emission in yellow (the contour levels of number counts of the smoothed full-band, 0.5–8 keV, image adopted from Lehmer et al. 2009 are 6, 9, 12, 15, 18, 21, 30, 40, and 50) are overlaid on the Ly α emission taken from Matsuda et al. (2004). Radio sources are labeled with letters in blue when more than one radio core is detected in one LAB. The offsets are relative to the centers of the LABs, denoted by blue crosses.

density of 0.91 ± 0.10 mJy at 350 GHz, coincident with the X-ray counterpart (Geach et al. 2009).

Our observation does not confirm the presence of a second continuum source (see Figure 4) marginally detected by Alexander et al. (2016) with a flux of 1.11 ± 0.25 mJy at 0.87 mm, which is significantly higher than our 3σ ALMA limit of 0.23 mJy. This may be due to the presence of extended

structure that is resolved out by our higher angular resolution observations or it may be a spurious source.

3.4.3. LAB3

The VLA data show a tentative detection within this LAB, but no dust emission is detected with SCUBA-2. Note that the

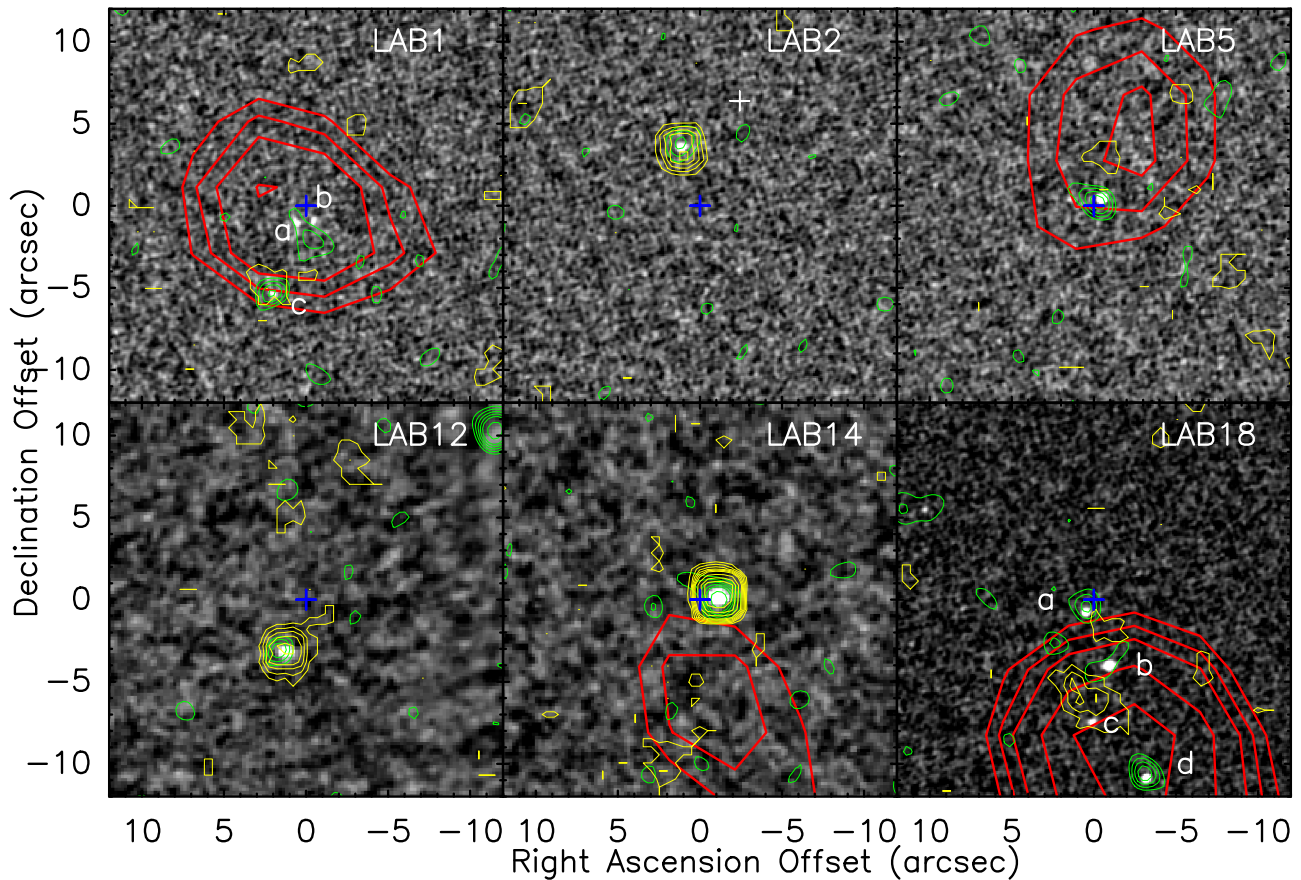


Figure 4. SCUBA2 dust emission at $850\ \mu\text{m}$ (red), VLA radio emission at 3 GHz (green) and *Chandra* X-ray emission (yellow) contours are overlaid on the continuum images (LAB12 and LAB14 at 1.14 mm and others at $850\ \mu\text{m}$) of the LABs observed with ALMA. The offsets are relative to the centers of the LABs. The contour levels are the same as in Figure 3. ALMA dust continuum sources are labeled with letters in white when more than one dust core is detected in a single LAB. The white cross in the panel of LAB2 denotes the location of dust continuum marginally detected at $870\ \mu\text{m}$ by Alexander et al. (2016).

radio peak has only a 3σ significance, and there are no counterparts at other wavelengths. Thus, the VLA signal might not be reliable, and we consider this LAB as undetected at radio frequencies. A strong X-ray source is detected in this LAB; however, it is not coincident with the weak radio peak.

Recently, dust continuum has been marginally detected around this LAB with ALMA (Alexander et al. 2016), but it is outside of the LAB, offset ~ 4.5 arcsec (~ 30 kpc) from the center. Thus, the dust continuum is not considered to be associated with the LAB.

3.4.4. LAB4

The radio emission peaks at the center of the LAB. However, the SCUBA-2 submillimeter source is offset 9 arcsec from the center. Considering the positional uncertainty of about 9 arcsec for this weak source, we still consider the submillimeter source to be consistent with the radio source and also associated with the LAB. A similar situation is encountered in LAB14, where the ALMA observations confirm the association between the radio and submillimeter sources. Note that there is a bright radio source at the southeastern edge (Figure 3). This is possibly a foreground source.

3.4.5. LAB5

This LAB is detected by SCUBA-2 and the VLA, and further confirmed by the ALMA observations. The SCUBA-2 and ALMA data show similar flux densities for this LAB.

3.4.6. LAB9

This LAB shows dust emission around the center. The VLA data reveal two radio components within this source, but only one source with an S/N above 4σ .

3.4.7. LAB10

This source is detected at submillimeter wavelengths with a significance of 3σ by SCUBA-2, but is not covered by our radio observations. Further cross-identification is needed to confirm its reliability.

3.4.8. LAB11

This LAB shows SCUBA-2 dust emission around the center. The marginally detected radio emission shows elongated structure, and its reality needs to be confirmed because of its low S/N .

3.4.9. LAB12

A significant radio detection is found within the LAB, but no dust counterpart is detected by SCUBA-2. However, the more sensitive ALMA observations at 1.14 mm show dust emission around the radio source. It also coincides with a strong X-ray counterpart (Geach et al. 2009). This LAB is also detected at 0.87 mm with ALMA by Alexander et al. (2016), showing a flux density of 1.58 ± 0.35 mJy. Both ALMA measurements

Table 3
Derived Star Formation Rates toward Submillimeter/Radio-detected LABs in SSA22

Source	SFR _{850 μm} ^a (M _⊙ yr ⁻¹)	Radio Comp	SFR _{10 cm} ^a	SFR _{10 cm} /SFR _{850 μm} (M _⊙ yr ⁻¹)	SFR _{Lyα} ^a (M _⊙ yr ⁻¹)	SFR _{Lyα} /SFR _{850 μm} (%)
SCUBA2-LAB1	376 ⁺³³² ₋₉₉	VLA-LAB1	1017 ± 198	2.7	68	18.1
ALMA-LAB1ab	140 ⁺¹²⁴ ₋₃₇	VLA-LAB1a	468 ± 140	3.3
ALMA-LAB1c	83 ⁺⁷³ ₋₂₂	VLA-LAB1b	549 ± 140	4.6
ALMA-LAB1	223 ⁺¹⁹⁷ ₋₅₉	VLA-LAB1	1017 ± 198	4.0	68	30.5
SCUBA2-LAB2	<195	VLA-LAB2	536 ± 156	>2.7	52	>26.5
ALMA-LAB2	118 ⁺¹⁰⁴ ₋₃₁	VLA-LAB2	536 ± 156	4.5	52	44.1
SCUBA2-LAB3 ^b	<237	...	<482	...	36	>14.9
SCUBA2-LAB4	317 ⁺²⁸⁰ ₋₈₄	VLA-LAB4a	1625 ± 264	5.1	23	7.4
		VLA-LAB4b	6342 ± 242
SCUBA2-LAB5	382 ⁺³³⁸ ₋₁₀₁	VLA-LAB5	690 ± 175	1.8	10	2.6
ALMA-LAB5	287 ⁺²⁵⁴ ₋₇₆	VLA-LAB5	690 ± 175	2.4	10	3.5
SCUBA2-LAB9	281 ⁺²⁴⁸ ₋₇₄	VLA-LAB9a	709 ± 215	2.5	8.0	2.9
		VLA-LAB9b	450 ± 218
SCUBA2-LAB10	349 ⁺³⁰⁸ ₋₉₂	14	3.9
SCUBA2-LAB11	302 ⁺²⁶⁶ ₋₈₀	VLA-LAB11	352 ± 172	1.2	5.6	1.8
SCUBA2-LAB12	<214	VLA-LAB12	474 ± 156	>2.2	5.3	>2.5
ALMA-LAB12	189 ⁺⁷⁶ ₋₁₉	VLA-LAB12	474 ± 156	2.5	5.3	2.7
SCUBA2-LAB14	265 ⁺²³⁴ ₋₇₀	VLA-LAB14	930 ± 137	3.5	7.4	2.8
ALMA-LAB14	389 ⁺²²⁷ ₋₆₃	VLA-LAB14	930 ± 137	2.4	7.4	1.9
SCUBA2-LAB16	309 ⁺²⁷³ ₋₈₂	VLA-LAB16	541 ± 170	1.7	6.1	2.0
SCUBA2-LAB18	696 ⁺⁶¹⁵ ₋₁₈₄	VLA-LAB18abd	2464 ± 462	3.5
ALMA-LAB18a	153 ⁺¹³⁵ ₋₄₀	VLA-LAB18a	830 ± 270	5.4	4.0	2.6
ALMA-LAB18b	355 ⁺³¹³ ₋₉₄	VLA-LAB18b	586 ± 254	1.7
ALMA-LAB18d	575 ⁺⁵⁰⁸ ₋₁₅₂	VLA-LAB18d	1048 ± 275	1.8

Notes.

^a The star formation rates (SFRs) are determined from measured submillimeter and radio fluxes under some assumptions (for details, see the text in Section 3.3. 2σ upper limits are given for submillimeter-undetected LABs.

^b Note that the LAB, not detected at dust and radio wavelengths but with X-ray emission, is also presented in this table.

can be well fitted by the SED templates described in Section 3.3

3.4.10. LAB14

The radio emission peaks around the center of the LAB, and SCUBA-2 shows dust emission centered 7 arcsec off the radio peak. However, our ALMA observations demonstrate that the 1.14 mm dust emission coincides with the radio counterpart (see Figure 4), supporting the reality of the SCUBA-2 detection. The inconsistency between the dust seen by SCUBA-2 and ALMA as well as the radio emission may be explained by the 1σ positional uncertainty of 9'' of the SCUBA-2 data. The radio source is also coincident with a strong X-ray counterpart (Geach et al. 2009).

This LAB was also detected at 0.87 mm by ALMA (Alexander et al. 2016), showing a flux density of 2.96 ± 0.29 mJy. The SED templates described in Section 3.3 can well fit both ALMA measurements. It predicts a flux density of 3.12 ± 0.31 at 0.85 mm, which is about 56% higher than the SCUBA-2 measurement, suggesting that SCUBA-2 only reveals about two-thirds of the total flux. It may be due to the effect of a negative sidelobe from a bright source in the south, which is 16'', close to the SCUBA-2 beam size of 14'', off the SCUBA-2 source associated with LAB14.

3.4.11. LAB16

The radio emission is detected around the center of the LAB and SCUBA-2 shows dust emission that peaks around 5 arcsec from the center, which is well within the 1σ positional uncertainty of the SCUBA-2 data.

3.4.12. LAB18

This is the strongest submillimeter source among all LABs in this field. The SCUBA-2 observations reveal a flux density of 5.4 ± 0.9 mJy. The ALMA observations discover four dust cores (a, b, c, and d in the lower right panel of Figure 4) with a total flux density of 9.47 ± 0.36 mJy, which is about 75% higher than the SCUBA-2 value. Three out of four ALMA submillimeter sources have radio counterparts. ALMA-LAB18a peaks around the center of the LAB and ALMA-LAB18b lies south of the center with an offset of 4.5 arcsec. The latter is surrounded by Lyα emission. If the Lyα emission in the south is a part of LAB18, its elongation along the north-south direction is around 13 arcsec, i.e., 100 kpc. The other two submillimeter sources, ALMA-LAB18c and ALMA-LAB18d, located farther to the south are outside the LAB and not associated with it. Geach et al. (2009) found an X-ray counterpart between two ALMA sources, ALMA-LAB18b and ALMA-LAB18c. However, the positional errors of the X-ray sources are expected to be the order of 2.5 arcsec in most

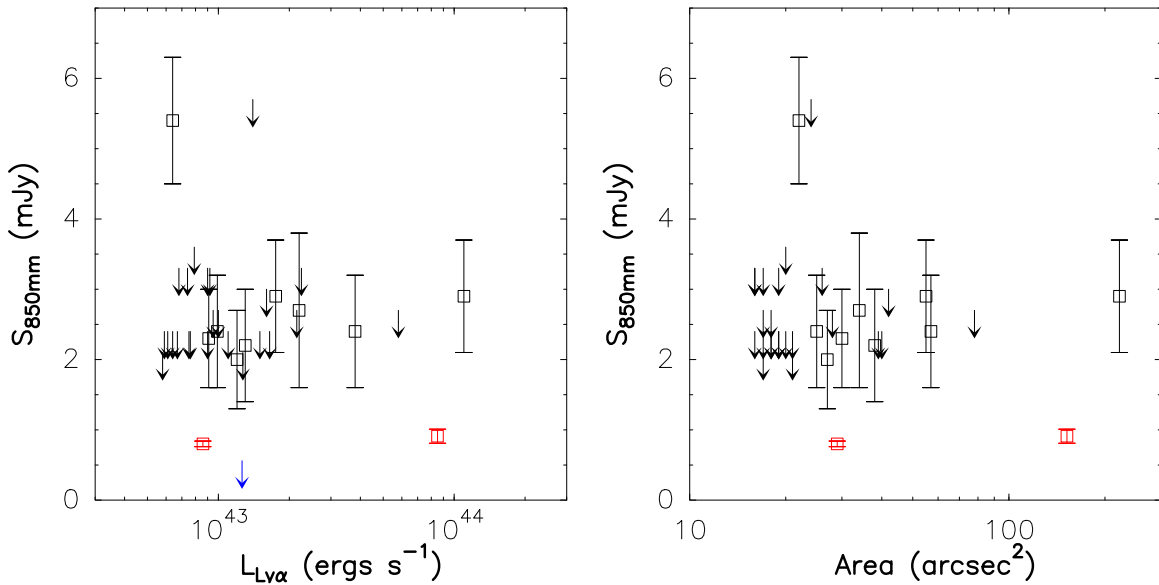


Figure 5. Distribution of measured 850 μm flux versus $\text{Ly}\alpha$ luminosity (left) and isophotal area (right) for the LABs in the SSA22 field. The black empty squares denote the LABs detected at 850 μm and the arrows mark undetected sources with 3σ upper limits. Two sources, LAB2 and LAB12, are only detected by ALMA with 850 μm fluxes less than 1.0 mJy, shown as red squares.

cases (Lehmer et al. 2009). LAB18 is at the edge of the X-ray image, and its positional error will be even larger. Therefore, the X-ray source might be associated with either ALMA-LAB18b or ALMA-LAB18c.

There is no continuum emission detected at 3.55 mm by Yang et al. (2014), showing a 3σ upper limit of 0.13 mJy. This is confirmed by the predicted flux density of $0.054_{-0.014}^{+0.048}$ mJy from the SED templates.

3.4.13. LAB30

There are four radio sources detected in this region (Figure 3). The sources, A, C, and D, show detections of high significance but are located outside of this LAB. Source D is found to be associated with a local galaxy at $z = 0.41$ (Saez et al. 2015). Source B is close to the center of the LAB, but only marginally detected at 3σ . No submillimeter emission is detected and the marginal detection of source B needs to be confirmed. We consider this source as undetected at radio wavelengths.

4. Discussion

4.1. Physical Sizes of LABs and Detection of Submillimeter Emission

Figure 5 shows the distribution of $\text{Ly}\alpha$ luminosity, isophotal area, and measured fluxes at submillimeter wavelengths for all LABs. In all 11 submillimeter-detected sources, 2 ALMA-detected LABs, LAB2 and LAB12, remain undetectable by our SCUBA-2 observations, while the remaining 9 sources are detected by SCUBA-2. In this section, we will therefore rely on the SCUBA-2 data alone to investigate possible relations between the physical size of LABs and the detection of submillimeter emission. In the left panel, we plot the submillimeter flux density against the $\text{Ly}\alpha$ luminosity. For the sources with $L_{\text{Ly}\alpha} > 10^{43} \text{ erg s}^{-1}$, 6 out of 17 LABs are detected at submillimeter wavelengths with SCUBA-2. For the fainter sources with $L_{\text{Ly}\alpha} < 10^{43} \text{ erg s}^{-1}$, 3 out of 18 LABs are detected at submm wavelengths. Apparently, more $\text{Ly}\alpha$

luminous galaxies are more likely to be detected at submillimeter wavelengths. In the right panel, we plot the submillimeter flux density against the isophotal area. For the first 18 large LABs, which are named according to their isophotal area in Matsuda et al. (2004), 9 are detected in the submillimeter. The remaining 17 LABs are not detected at submillimeter wavelengths. This suggests that large LABs exhibit stronger submillimeter emission. Furthermore, our results suggest that the detection of submillimeter dust emission in LABs is more linked to the physical sizes of $\text{Ly}\alpha$ emission than to their $\text{Ly}\alpha$ luminosities. The physical sizes of $\text{Ly}\alpha$ emission, instead of their luminosities, may have a tight correlation with dust emission. This seems to be inconsistent with the fairly tight correlation between the physical sizes of LABs and the $\text{Ly}\alpha$ luminosities reported by Matsuda et al. (2004). However, one should note that the correlation is weak if excluding the four brightest/largest LABs. The (sub) millimeter emission can be a good indicator of gas masses for SMGs because of its low optical depth. Due to the uncertainties in the $\text{Ly}\alpha$ escape fraction of LABs, the $\text{Ly}\alpha$ emission is not a good mass tracer of SMGs and therefore the correlation between the dust emission and the $\text{Ly}\alpha$ emission is not very tight. The larger physical extension of $\text{Ly}\alpha$ emission may be related to spatially more extended surrounding atomic hydrogen and star-forming regions emitting ionizing photons. A recent study (Matsuda et al. 2012) shows that the spatial extent of the $\text{Ly}\alpha$ haloes is determined by the surrounding megaparsec-scale environment, rather than by the central UV luminosities. However, this is inconsistent with the result in Xue et al. (2017), who do not find any correlation between measured scale-lengths and degree of overdensity relative to the environment. It is worth emphasizing that the trend to dust detections, more related to LAB sizes than to LAB luminosities, is based not entirely on detections but on detections of the large area LABs and nondetection of the smaller area LABs. Future more sensitive ALMA data may settle this puzzle and reveal the relation between LAB sizes and their possible internal heating sources in a more convincing way.

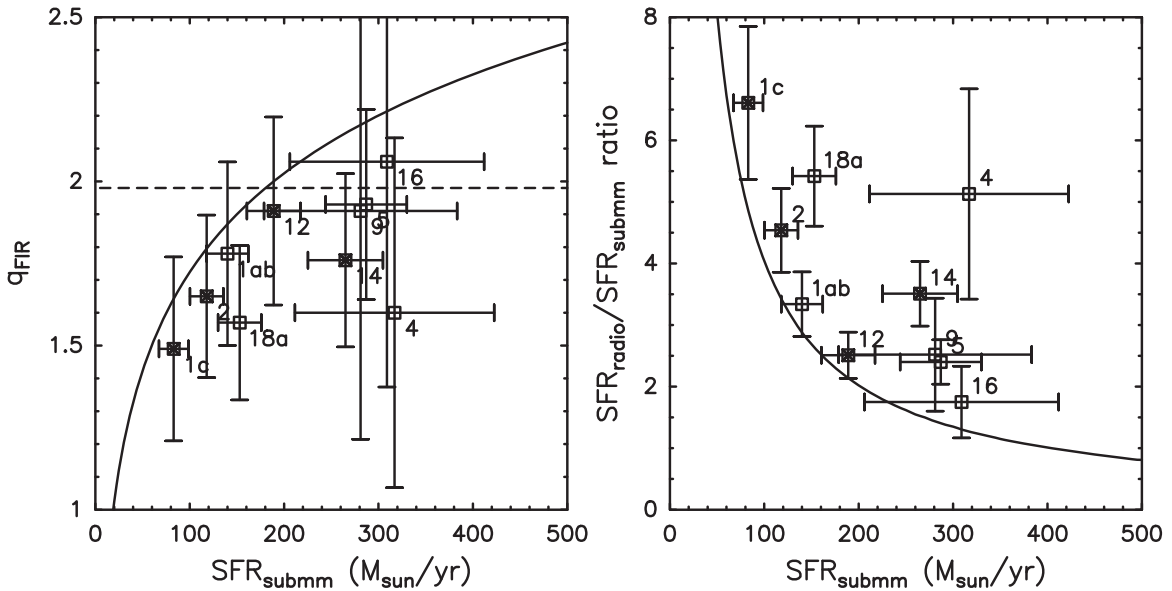


Figure 6. Parametrization of the FRC, q_{FIR} , (left) and $\text{SFR}_{\text{radio}}/\text{SFR}_{\text{submm}}$ ratios (right) against $\text{SFR}_{\text{submm}}$ for the LABs detected at dust and radio wavelengths. The sources detected in X-rays are shown with cross symbols inside the open squares. The solid lines present the detection limit, corresponding to a radio flux of $6.3 \mu\text{Jy}$, constrained by the VLA observations. The dashed line in the left panel denotes the q_{FIR} value at $z = 3.1$ predicted by the redshift evolution of q_{FIR} in Magnelli et al. (2015).

4.2. Powering Sources of LABs: Star Formation or Active Galactic Nuclei?

4.2.1. Submillimeter and Radio Detections in LABs and Their Implications on Heating Mechanisms

The heating mechanism of LABs is still unclear. About one-third of the LABs in SSA22 are associated with submillimeter/radio sources with SFRs above $100 M_{\odot} \text{yr}^{-1}$. Spectroscopic measurements from the literature (see Table 2) confirm that at least some of the detected submillimeter/radio counterparts are indeed associated with the LABs. These results suggest that internal heating in the host galaxies may be a major energy source for some LABs. It is consistent with our recent study of J2143–4423 (Ao et al. 2015), where 2 out of 4 LABs have been detected at radio and submillimeter wavelengths.

Alternately, AGNs may also be responsible for heating the gas. Deep *Chandra* X-ray observations in the SSA 22 field (Geach et al. 2009; Lehmer et al. 2009) cover 29 LABs. Indeed, 6 out of 29 LABs have X-ray counterparts, implying a significant fraction of AGNs in LABs. Among these, six X-ray detected LABs, LAB3 shows no counterparts at radio and submillimeter wavelengths (for details, see Section 3.4 and Figure 3) and LAB18 is not clearly associated with any submillimeter/radio counterparts, given the pointing accuracy of the *Chandra* observations (for details, see Section 3.4 and Figures 3 and 4). The remaining four LABs, LAB2, LAB12, and LAB14, identified in Geach et al. (2009), as well as LAB1 with weak X-ray emission (see Figure 4), are detected at radio and submillimeter wavelengths.

The far-infrared (FIR) and radio luminosities of star-forming galaxies are tightly related via an empirical relationship, the FIR/radio correlation (FRC; e.g., Helou et al. 1988; Yun et al. 2001; Magnelli et al. 2015). The radio excess in the systems with AGNs drives them to deviate from this tight relationship. Therefore, following the method described in Magnelli et al. (2015), we use the parametrization of the FRC, q_{FIR} , to study the radio excess in our sample. The q_{FIR}

parameter is defined as

$$q_{\text{FIR}} = \log \left(\frac{L_{\text{FIR}} [\text{W}]}{3.75 \times 10^{12}} \right) - \log(L_{1.4 \text{ GHz}} [\text{W Hz}^{-1}]) \quad (1)$$

(e.g., Helou et al. 1988; Yun et al. 2001; Magnelli et al. 2015), where L_{FIR} is the integrated FIR luminosity from rest-frame 42 to $122 \mu\text{m}$ and $L_{\text{IR}} = 1.91 \times L_{\text{FIR}}$ (Magnelli et al. 2015), and $L_{1.4 \text{ GHz}}$ is the rest-frame 1.4 GHz radio luminosity and is calculated as in Section 3.3. The results are shown in the left panel of Figure 6. We also compare our results to the q_{FIR} value at $z = 3.1$ predicted by the redshift evolution of q_{FIR} in Magnelli et al. (2015). The detection limit set by the sensitivity of VLA observations is shown as the solid line in Figure 6. It is clear that all X-ray detected LABs have q_{FIR} below the predicted value. For the sources detected at both submillimeter and radio wavelengths, 8 out of 10 LABs have q_{FIR} lower than the predicted value for the star-forming galaxies, suggesting a radio excess in LABs is common. In the right panel of Figure 6, we plot $\text{SFR}_{\text{radio}}/\text{SFR}_{\text{submm}}$ ratios against $\text{SFR}_{\text{submm}}$. It is clear that X-ray detected LABs have $\text{SFR}_{\text{radio}}/\text{SFR}_{\text{submm}}$ ratios above 2.5. For the sources detected at both submillimeter and radio wavelengths, 8 out of 10 LABs have ratios larger than 2.5, suggesting that a radio excess in LABs is common. Previously taken radio/FIR data from local AGNs (Rush et al. 1993, 1996) show that Seyfert galaxies have a three times stronger 6 cm radio continuum than predicted by star formation alone, indicating that the existence of AGNs in submillimeter/radio-detected LABs might be common. This is consistent with the finding that 10 out of 12 LAEs with $L_{\text{Ly}\alpha} > 10^{43} \text{ erg s}^{-1}$ are detected in X-rays with *Chandra* (Civano et al. 2016; Sobral et al. 2017). However, it is very difficult to discriminate between predominately SF or AGN powered LABs. At least for the submillimeter/radio-detected sources with SFRs larger than $100 M_{\odot} \text{yr}^{-1}$, it is very likely that SF is an important heating

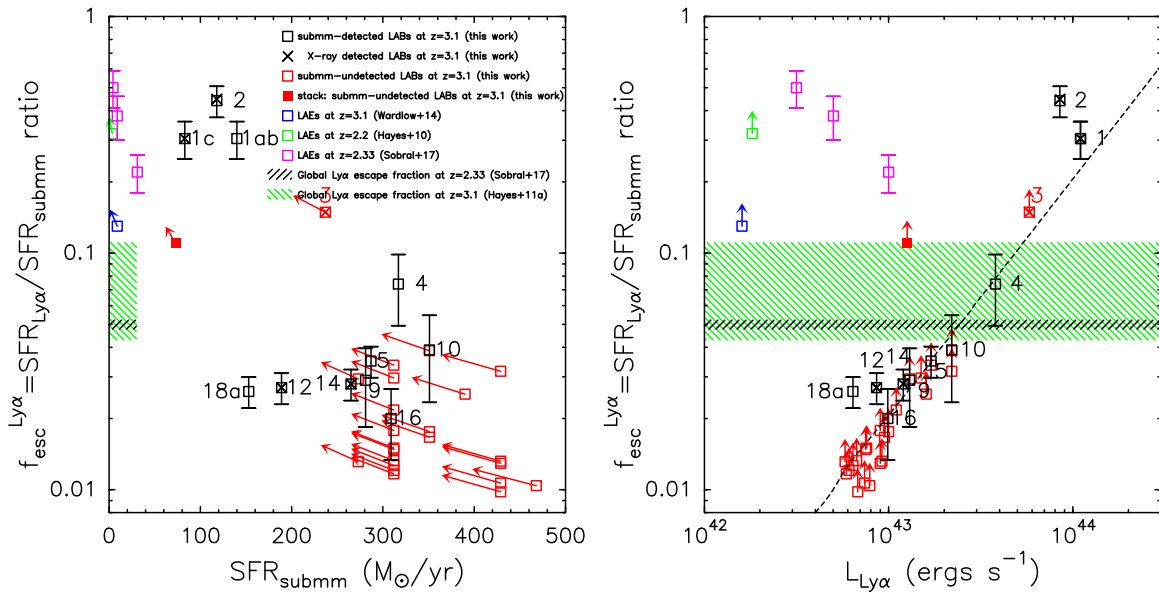


Figure 7. Plots of the escape fraction, $f_{\text{esc}}^{\text{Ly}\alpha}$, against the star formation rate (left) and $\text{Ly}\alpha$ luminosity (right). Submillimeter-detected and submillimeter-undetected LABs are marked by black and red squares, respectively. Stacked submillimeter-undetected LABs are presented by a filled red square. X-ray detected LABs are indicated by crosses inside the squares. Lower limits of $f_{\text{esc}}^{\text{Ly}\alpha}$ for LAEs at $z = 2.2$ and 3.1 are presented in green (Hayes et al. 2010) and blue (Wardlow et al. 2014), respectively. The fractions for LAEs at $z = 2.23$ in Sobral et al. (2017) are shown in magenta. The global $\text{Ly}\alpha$ escape fractions at $z = 2.33$ (Sobral et al. 2017) and $z = 3.1$ (Hayes et al. 2011a) are denoted by black and green hashed regions, respectively, where their typical SFRs are less than $20 M_{\odot} \text{yr}^{-1}$. The dashed line in the right panel denotes the lower limit of $f_{\text{esc}}^{\text{Ly}\alpha}$ constrained by the SCUBA-2 detection threshold of $300 M_{\odot} \text{yr}^{-1}$. Some detected sources above this line are due to better sensitivities of the ALMA measurements. Some undetected LABs, shown as red open squares at 3σ , well below the line are limited by their poor sensitivities outside the central field of the SCUBA-2 observations.

mechanism, and among most of them AGNs may also play an important role in powering the $\text{Ly}\alpha$ emission.

Note that the upper SFR limits of the submillimeter-undetected sources by the SCUBA-2 measurements are about $300 M_{\odot} \text{yr}^{-1}$, which is usually much higher than the SFR determined by the $\text{Ly}\alpha$ luminosity. Therefore, it is difficult to draw a strong conclusion on the powering sources of these LABs with the current data, due to the large variance in the $\text{Ly}\alpha$ escape fraction (see Section 4.3). Future deep observations are required to settle this problem.

4.2.2. Locations of Radio and X-Ray Counterparts within LABs and Their Implications on Heating Mechanisms

Due to the limited angular resolution and positional uncertainties of the SCUBA-2 observations, it is impossible to pinpoint the accurate positions of the SMGs in the LABs with SCUBA-2 data alone. With the high angular resolution VLA images, the accurate positions of radio counterparts and their associated SMGs are now well determined. Among the sources with radio counterparts detected above 4σ , four LABs, LAB4, LAB5, LAB9, and LAB16, have no X-ray counterparts. Except for LAB9, the radio counterparts of the remaining three sources, LAB4, LAB5, and LAB16, are located in the center of the LABs. This may provide evidence in support of SF as the main powering source in these LABs, and is consistent with the SF-based model (e.g., Zheng et al. 2011) for LAB formation and recent observations by Matsuda et al. (2012) who find that stacking of fainter LAEs in the SSA 22 field shows the extended and faint $\text{Ly}\alpha$ emission surrounding the bright sources at the center. However, the existence of AGNs in these LABs cannot be excluded. Especially, LAB4 has a high $\text{SFR}_{\text{radio}}/\text{SFR}_{\text{submm}}$ ratio of 5.1 ± 1.7 , strongly supporting that an AGN may reside there. Thus, these sources without X-ray

emission may also host AGNs, but still deeply embedded in their host galaxies where X-ray emission might be efficiently absorbed. This is supported by the fact that these four LABs contain the high massive dust masses among all LABs.

X-ray emission has been detected in 6 of the 29 LABs of the SSA22 field. This includes LAB1, not discussed in Geach et al. (2009), suggesting the existence of AGNs in these systems. None of the X-ray sources are located at the LAB's center. This positional inconsistency between $\text{Ly}\alpha$ and the embedded AGNs has already previously been found in a few LABs (Prescott et al. 2013; Yang et al. 2014). In comparison with the X-ray detected LABs, the LABs with the radio counterparts in the centers usually contain more material and they are located in the centers of the LABs. It is possible that their X-ray emission, if present, is largely absorbed by neutral hydrogen, helium, and presumably recently synthesized heavy elements. Alternatively, a recent simulation (Geach et al. 2016) shows that observed $\text{Ly}\alpha$ surface brightness and morphology is highly orientation dependent. This may lead to positional inconsistencies between X-ray sources and the centers of LABs. However, this simulation cannot explain why most radio counterparts without X-ray emission locate at the centers of LABs.

4.3. $\text{Ly}\alpha$ Escape Fraction at $z = 3.1$

It is very interesting to know the $\text{Ly}\alpha$ escape fraction, $f_{\text{esc}}^{\text{Ly}\alpha}$, in LABs, a special class of LAEs, and to understand it in different environments. Traditionally, the $\text{Ly}\alpha$ escape fraction at $z \geq 2.3$ is mainly derived from the $\text{Ly}\alpha$ and UV/H α luminosity function (e.g., Hayes et al. 2011a; Sobral et al. 2017). Dust emission is directly related to SF activity in galaxies and has been widely used as a good SFR estimator (Kennicutt 1998; Kennicutt & Evans 2012). Therefore, using SCUBA-2/ALMA data, the $\text{Ly}\alpha$ escape fraction can also be

calculated from the ratio of Ly α to dust continuum derived SFRs. In Figure 7, we plot $f_{\text{esc}}^{\text{Ly}\alpha}$ against the SFRs and Ly α luminosities of the LABs. The Ly α escape fraction ranges from 2% to 45% among the submillimeter-detected LABs, with a median value of about 3%. Except for 11 submillimeter-detected sources, the remaining LABs not detected at submillimeter wavelengths can also provide important constraints on $f_{\text{esc}}^{\text{Ly}\alpha}$. Lower limits of $f_{\text{esc}}^{\text{Ly}\alpha}$ can be estimated by using the upper limits of SCUBA-2 measurements and these values are presented in Figure 7. We also stack the submillimeter-undetected LABs, but fail to detect the dust emission at $>3\sigma$, leading to a lower limit of $f_{\text{esc}}^{\text{Ly}\alpha}$ to be 11%. This suggests that the majority of the sample have higher $f_{\text{esc}}^{\text{Ly}\alpha}$ in comparison with the global Ly α escape fraction in the previous studies (Hayes et al. 2011a; Sobral et al. 2017), where the global escape fraction refers to the value for all galaxies in a field, and is usually determined from the integral of the Ly α and H α luminosity functions. Indeed, the fractions in the LAEs are usually much higher than the global values, as the LAEs are a biased sample, selected by their strong Ly α emission. Hayes et al. (2010) reported $f_{\text{esc}}^{\text{Ly}\alpha} > 32\%$ for LAEs at $z = 2.2$, Sobral et al. (2017) shows that $f_{\text{esc}}^{\text{Ly}\alpha}$ is around 37% for LAEs at $z = 2.23$. Wardlow et al. (2014) use far-infrared data instead of optical data and obtain a lower limit of $f_{\text{esc}}^{\text{Ly}\alpha}$ to be 10% to 20% for LAEs at $z = 3.1$, which is consistent with our stacking results for the majority of the LABs.

We notice that most submillimeter-detected LABs have Ly α escape fractions much lower than the fractions of LAEs in other studies (e.g., Hayes et al. 2010; Wardlow et al. 2014; Sobral et al. 2017), as shown in Figure 7. We find a big difference between these LABs and those of Hayes et al. (2010), Wardlow et al. (2014), and Sobral et al. (2017) that the SFRs of the submillimeter-detected LABs are much higher than those in the latter three samples. The galaxies with high SFRs are most likely massive galaxies with a large amount of dust. We suspect that the low Ly α escape fractions in the submillimeter-detected LABs are probably due to high dust attenuation as their SFRs are about one magnitude higher than in the samples of other studies. Another reason may be related to the large-scale environment around the LABs. All sources are located in the dense region of SSA 22, which contains a large amount of circumgalactic medium. In such an environment, Ly α photons experience numerous resonance scatterings, and can also be easily absorbed by surrounding neutral hydrogen atoms, making the Ly α emission more extended and leading to a lower escape fraction. This is consistent with the recent study of Shimakawa et al. (2017), who find that Ly α escape fractions in high-density regions are lower than in low-density regions. We also note that three LABs, LAB1, LAB2, and LAB3, have similar Ly α escape fractions as the LAEs studied by Hayes et al. (2010), Wardlow et al. (2014), and Sobral et al. (2017). All of these sources have X-ray emission. Their high fractions may be partially due to the AGNs in the host galaxies. The AGNs will produce additional photons and feedback to possibly remove the material surrounding the centers and then enhance the Ly α emission by increasing the escaping photons from the central regions. We also need to mention that our SCUBA-2 data provide superior measures of SFRs from extinction-free dust emission, in comparison with typically used optical data that suffer large uncertainties due to the extinction correction. The actual escape fractions will decrease if considering an extra extinction related to the H II regions

for H α (Wuyts et al. 2013; Reddy et al. 2015, 2016; An et al. 2017). To better understand the physical origin of the low Ly α escape fraction in the LABs, deep submillimeter observations will be useful.

5. Conclusions

We have presented submillimeter data from JCMT/SCUBA-2 observations together with ALMA data toward 35 LABs identified in the SSA22 field by Matsuda et al. (2004) and deep radio images with the VLA toward 29 out of the 35 LABs. We also discuss the deep X-ray data from the same region. Our conclusions are as follows.

1. With the JCMT/SCUBA-2 and ALMA, 11 out of 35 LABs show dust emission. With the VLA, 9 out of 29 LABs are detected at radio wavelengths. For 5 out of the 9 radio-detected sources, spectroscopic data from the literature reveal redshifts around 3.1, confirming that the radio counterparts and the corresponding submm sources are associated with the LABs.
2. The detection of submillimeter dust emission in LABs is more linked to the physical sizes of Ly α emission than their Ly α luminosities.
3. The 11 LABs detected at submillimeter wavelengths have SFRs over $100 M_{\odot} \text{ yr}^{-1}$, favoring star formation as an important energy source for some LABs. Our results show that a radio excess is common in the submillimeter/radio-detected LABs and therefore AGNs may also play an important role to power the Ly α emission.
4. Among the four radio-detected LABs lacking X-ray emission, three sources are located in the center of their parent LABs. All X-ray sources are not located at the center of their associated LABs. The latter may be explained by absorption due to neutral hydrogen, helium, and potentially newly formed heavy elements or by LAB morphologies, which are highly orientation dependent.
5. The Ly α escape fraction ranges from 2% to 45% among the submillimeter-detected LABs, with a median value of about 3%. Based on the stacked data, the submillimeter-undetected LABs show a lower limit of 11%, which is consistent with those of LAEs in previous studies. However, some submillimeter-detected LABs have significantly lower Ly α escape fractions. We suspect that this large variation in Ly α escape fractions is due to the high dust attenuation supported by the large SFRs in our sample, the dense large-scale environment in SSA22 as well as large uncertainties related to the extinction correction in optical data.

We thank the anonymous referee for valuable comments that improved this manuscript. Y.A. thanks Fangxia An for the comment about the effect of extinction correction on the Ly α escape fraction and Thomas Reiprich for the discussion about the contributions to the X-ray emission. Y.A. was supported by the ALMA Japan Research Grant of NAOJ Chile Observatory, NAOJ-ALMA-0165. Y.A. acknowledges partial support by NSFC grant 11373007 and Youth Innovation Promotion Association CAS. M.H. acknowledges the support of the Swedish Research Council, Vetenskapsrådet and the Swedish National Space Board (SNSB), and is Fellow of the Knut and Alice Wallenberg Foundation. N.K.H. is supported by the Science and Technology Facilities Council (grant number ST/K502029/1).

The James Clerk Maxwell Telescope has historically been operated by the Joint Astronomy Centre on behalf of the Science and Technology Facilities Council of the United Kingdom, the National Research Council of Canada and the Netherlands Organisation for Scientific Research. Additional funds for the construction of SCUBA-2 were provided by the Canada Foundation for Innovation. The James Clerk Maxwell Telescope is operated by the East Asian Observatory on behalf of The National Astronomical Observatory of Japan, Academia Sinica Institute of Astronomy and Astrophysics, the Korea Astronomy and Space Science Institute, the National Astronomical Observatories of China and the Chinese Academy of Sciences (Grant No. XDB09000000), with additional funding support from the Science and Technology Facilities Council of the United Kingdom and participating universities in the United Kingdom and Canada.

This paper makes use of the following ALMA data: ADS/JAO.ALMA#2013.1.00162.S and ADS/JAO.ALMA#2013.1.00704.S. ALMA is a partnership of ESO (representing its member states), NSF (USA) and NINS (Japan), together with NRC (Canada), NSC, and ASIAA (Taiwan), and KASI (Republic of Korea), in cooperation with the Republic of Chile. The Joint ALMA Observatory is operated by ESO, AUI/NRAO, and NAOJ.

ORCID iDs

Y. Ao  <https://orcid.org/0000-0003-3139-2724>
 C. Henkel  <https://orcid.org/0000-0002-7495-4005>
 D. Iono  <https://orcid.org/0000-0002-2364-0823>
 D. M. Alexander  <https://orcid.org/0000-0002-5896-6313>
 B. Hatsukade  <https://orcid.org/0000-0001-6469-8725>
 N. K. Hine  <https://orcid.org/0000-0002-7975-0474>
 R. Kawabe  <https://orcid.org/0000-0002-8049-7525>
 K. Kohno  <https://orcid.org/0000-0002-4052-2394>
 M. Lehnert  <https://orcid.org/0000-0003-1939-5885>
 M. Malkan  <https://orcid.org/0000-0001-6919-1237>
 K. M. Menten  <https://orcid.org/0000-0001-6459-0669>
 M. Ouchi  <https://orcid.org/0000-0002-1049-6658>
 A. Weiss  <https://orcid.org/0000-0003-4678-3939>

References

- Alexander, D. M., Simpson, J. M., Harrison, C. M., et al. 2016, *MNRAS*, 461, 2944
 An, F. X., Zheng, X. Z., Hao, C.-N., Huang, J.-S., & Xia, X.-Y. 2017, *ApJ*, 835, 116
 Ao, Y., Matsuda, Y., Beelen, A., et al. 2015, *A&A*, 581, A132
 Bell, E. F. 2003, *ApJ*, 586, 794
 Bridge, C. R., Blain, A., Borys, C. J. K., et al. 2013, *ApJ*, 769, 91
 Cen, R., & Zheng, Z. 2013, *ApJ*, 775, 112
 Chapin, E. L., Berry, D. S., Gibb, A. G., et al. 2013, *MNRAS*, 430, 2545
 Civano, F., Marchesi, S., Comastri, A., et al. 2016, *ApJ*, 819, 62
 Colbert, J. W., Teplitz, H., Francis, P., et al. 2006, *ApJL*, 637, L89
 Condon, J. J., Cotton, W. D., Fomalont, E. B., et al. 2012, *ApJ*, 758, 23
 Condon, J. J., Cotton, W. D., Greisen, E. W., et al. 1998, *AJ*, 115, 1693
 Dey, A., Bian, C., Soifer, B. T., et al. 2005, *ApJ*, 629, 654
 Dijkstra, M., & Loeb, A. 2009, *MNRAS*, 400, 1109
 Erb, D. K., Bogosavljević, M., & Steidel, C. C. 2011, *ApJL*, 740, L31
 Faucher-Giguère, C.-A., Kereš, D., Dijkstra, M., Hernquist, L., & Zaldarriaga, M. 2010, *ApJ*, 725, 633
 Francis, P. J., Woodgate, B. E., Warren, S. J., et al. 1996, *ApJ*, 457, 490
 Furlanetto, S. R., Schaye, J., Springel, V., & Hernquist, L. 2005, *ApJ*, 622, 7
 Geach, J. E., Alexander, D. M., Lehmer, B. D., et al. 2009, *ApJ*, 700, 1
 Geach, J. E., Bower, R. G., Alexander, D. M., et al. 2014, *ApJ*, 793, 22
 Geach, J. E., Dunlop, J. S., Halpern, M., et al. 2017, *MNRAS*, 465, 1789
 Geach, J. E., Matsuda, Y., Smail, I., et al. 2005, *MNRAS*, 363, 1398
 Geach, J. E., Narayanan, D., Matsuda, Y., et al. 2016, *ApJ*, 832, 37
 Gronwall, C., Ciardullo, R., Hickey, T., et al. 2007, *ApJ*, 667, 79
 Haiman, Z., Spaans, M., & Quataert, E. 2000, *ApJL*, 537, L5
 Hayes, M. 2015, *PASA*, 32, e027
 Hayes, M., Östlin, G., Schaerer, D., et al. 2010, *Natur*, 464, 562
 Hayes, M., Scarlata, C., & Siana, B. 2011, *Natur*, 476, 304
 Hayes, M., Schaerer, D., Östlin, G., et al. 2011, *ApJ*, 730, 8
 Helou, G., Khan, I. R., Malek, L., & Boehmer, L. 1988, *ApJS*, 68, 151
 Hine, N. K., Geach, J. E., Matsuda, Y., et al. 2016, *MNRAS*, 460, 4075
 Holland, W. S., Bintley, D., Chapin, E. L., et al. 2013, *MNRAS*, 430, 2513
 Ivison, R. J., Magnelli, B., Ibar, E., et al. 2010, *A&A*, 518, L31
 Kennicutt, R. C., & Evans, N. J. 2012, *ARA&A*, 50, 531
 Kennicutt, R. C., Jr. 1998, *ARA&A*, 36, 189
 Kubo, M., Uchimoto, Y. K., Yamada, T., et al. 2013, *ApJ*, 778, 170
 Kubo, M., Yamada, T., Ichikawa, T., et al. 2015, *ApJ*, 799, 38
 Lehmer, B. D., Alexander, D. M., Chapman, S. C., et al. 2009, *MNRAS*, 400, 299
 Magnelli, B., Ivison, R. J., Lutz, D., et al. 2015, *A&A*, 573, A45
 Matsuda, Y., Iono, D., Ohta, K., et al. 2007, *ApJ*, 667, 667
 Matsuda, Y., Nakamura, Y., Morimoto, N., et al. 2009, *MNRAS*, 400, L66
 Matsuda, Y., Yamada, T., Hayashino, T., et al. 2004, *AJ*, 128, 569
 Matsuda, Y., Yamada, T., Hayashino, T., et al. 2011, *MNRAS*, 410, L13
 Matsuda, Y., Yamada, T., Hayashino, T., et al. 2012, *MNRAS*, 425, 878
 Mori, M., & Umemura, M. 2006, *Natur*, 440, 644
 Nilsson, K. K., Fynbo, J. P. U., Møller, P., Sommer-Larsen, J., & Ledoux, C. 2006, *A&A*, 452, L23
 Ouchi, M., Shimasaku, K., Akiyama, M., et al. 2008, *ApJS*, 176, 301
 Overzier, R. A., Nesvadba, N. P. H., Dijkstra, M., et al. 2013, *ApJ*, 771, 89
 Palunas, P., Teplitz, H. I., Francis, P. J., Williger, G. M., & Woodgate, B. E. 2004, *ApJ*, 602, 545
 Prescott, M. K. M., Dey, A., Brodwin, M., et al. 2012, *ApJ*, 752, 86
 Prescott, M. K. M., Dey, A., & Jannuzi, B. T. 2012, *ApJ*, 748, 125
 Prescott, M. K. M., Dey, A., & Jannuzi, B. T. 2013, *ApJ*, 762, 38
 Prescott, M. K. M., Momcheva, I., Brammer, G. B., Fynbo, J. P. U., & Møller, P. 2015, *ApJ*, 802, 32
 Reddy, N. A., Kriek, M., Shapley, A. E., et al. 2015, *ApJ*, 806, 259
 Reddy, N. A., Steidel, C. C., Pettini, M., & Bogosavljević, M. 2016, *ApJ*, 828, 107
 Rush, B., Malkan, M. A., & Edelson, R. A. 1996, *ApJ*, 473, 130
 Rush, B., Malkan, M. A., & Spinoglio, L. 1993, *ApJS*, 89, 1
 Saez, C., Lehmer, B. D., Bauer, F. E., et al. 2015, *MNRAS*, 450, 2615
 Saito, T., Shimasaku, K., Okamura, S., et al. 2006, *ApJ*, 648, 54
 Shimakawa, R., Kodama, T., Hayashi, M., et al. 2017, *MNRAS*, 468, L21
 Silva, L., Granato, G. L., Bressan, A., & Danese, L. 1998, *ApJ*, 509, 103
 Smith, D. J. B., & Jarvis, M. J. 2007, *MNRAS*, 378, L49
 Sobral, D., Matthee, J., Best, P., et al. 2017, *MNRAS*, 466, 1242
 Steidel, C. C., Adelberger, K. L., Shapley, A. E., et al. 2000, *ApJ*, 532, 170
 Steidel, C. C., Adelberger, K. L., Shapley, A. E., et al. 2003, *ApJ*, 592, 728
 Swinbank, A. M., Simpson, J. M., Smail, I., et al. 2014, *MNRAS*, 438, 1267
 Swinbank, A. M., Smail, I., Longmore, S., et al. 2010, *Natur*, 464, 733
 Tamura, Y., Kohno, K., Nakanishi, K., et al. 2009, *Natur*, 459, 61
 Tamura, Y., Matsuda, Y., Ikarashi, S., et al. 2013, *MNRAS*, 430, 2768
 Taniguchi, Y., & Shioya, Y. 2000, *ApJL*, 532, L13
 Umehata, H., Matsuda, Y., Tamura, Y., et al. 2017a, *ApJL*, 834, L16
 Umehata, H., Tamura, Y., Kohno, K., et al. 2014, *MNRAS*, 440, 3462
 Umehata, H., Tamura, Y., Kohno, K., et al. 2015, *ApJL*, 815, L8
 Umehata, H., Tamura, Y., Kohno, K., et al. 2017b, *ApJ*, 835, 98
 Wardlow, J. L., Malhotra, S., Zheng, Z., et al. 2014, *ApJ*, 787, 9
 Webb, T. M. A., Yamada, T., Huang, J.-S., et al. 2009, *ApJ*, 692, 1561
 Wilman, R. J., Gersten, J., Bower, R. G., et al. 2005, *Natur*, 436, 227
 Wuyts, S., Förster Schreiber, N. M., Nelson, E. J., et al. 2013, *ApJ*, 779, 135
 Xue, R., Lee, K.-S., Dey, A., et al. 2017, *ApJ*, 837, 172
 Yajima, H., Li, Y., & Zhu, Q. 2013, *ApJ*, 773, 151
 Yamada, T., Matsuda, Y., Kousai, K., et al. 2012, *ApJ*, 751, 29
 Yang, Y., Decarli, R., Dannerbauer, H., et al. 2012, *ApJ*, 744, 178
 Yang, Y., Walter, F., Decarli, R., et al. 2014, *ApJ*, 784, 171
 Yang, Y., Zabludoff, A., Eisenstein, D., & Davé, R. 2010, *ApJ*, 719, 1654
 Yang, Y., Zabludoff, A., Tremonti, C., Eisenstein, D., & Davé, R. 2009, *ApJ*, 693, 1579
 Yun, M. S., Reddy, N. A., & Condon, J. J. 2001, *ApJ*, 554, 803
 Zheng, Z., Cen, R., Weinberg, D., Trac, H., & Miralda-Escudé, J. 2011, *ApJ*, 739, 62